Nathan A. Pehrson
Department of Mechanical Engineering,
Brigham Young University,
Provo, UT 84602
e-mail: napehrson@byu.edu

Pietro Bilancia
Department of Mechanical, Energy, Management
and Transportation Engineering,
University of Genova,
Genova 16145, Italy
e-mail: pietro.bilancia@edu.unige.it

Spencer Magleby
Department of Mechanical Engineering,
Brigham Young University,
Provo, UT 84602
e-mail: magleby@byu.edu

Larry Howell
Department of Mechanical Engineering,
Brigham Young University,
Provo, UT 84602
e-mail: lhowell@byu.net

Load–Displacement Characterization in Three Degrees-of-Freedom for General Lamina Emergent Torsion Arrays

Lamina emergent torsion (LET) joints for use in origami-based applications enables folding of panels. Placing LET joints in series and parallel (formulating LET arrays) opens the design space to provide for tunable stiffness characteristics in other directions while maintaining the ability to fold. Analytical equations characterizing the elastic load–displacement for general serial–parallel formulations of LET arrays for three degrees-of-freedom are presented: rotation about the desired axis, in-plane rotation, and extension/compression. These equations enable the design of LET arrays for a variety of applications, including origami-based mechanisms. These general equations are verified using finite element analysis, and to show variability of the LET array design space, several verification plots over a range of parameters are provided. [DOI: 10.1115/1.4046072]

Keywords: compliant mechanisms, lamina emergent mechanisms, lamina emergent torsion (LET) joints, compliant joints, finite element analysis

1 Introduction

Lamina emergent mechanisms (LEMs) are compliant mechanisms formed from a planar material and have some or all of their motion out of the plane [1–8]. They can be fabricated using two-dimensional processes and rely on the compliance of flexible members formed from the planar material to gain their motion [9]. Apart from common benefits of compliant mechanisms such as high precision, the absence of backlash and wear, and the limited amount of parts [9], LEMs are characterized by a low manufacturing cost, a relatively simple topology, and compactness in the initial state. Characterization of the load–displacement behavior of LEMs is an important step to appropriately design mechanisms with desirable behaviors. They have been used in a variety of applications, including microelectromechanical systems [1,10] and origami-based mechanisms [11,12]. A particularly useful LEM for origami-based mechanisms is the lamina emergent torsion (LET) joint. The LET joint achieves high rotational compliance while minimizing the required footprint of the joint, allowing for origami-like folding of panels and localized joints [13–15]. Recent studies have provided many folding and modeling techniques (e.g., elastic origami models [16], truss frameworks [17], topology optimization [18], and mechanical properties of paper folds [19]) and applications (e.g., kinetogami [20], deformable structures [21], and cylinders [22]) for origami-based mechanisms. Systems of panels and low-footprint joint designs are beneficial for applications where the function of the panels depends on the panel size. This feature can be used to create networks of monolithic panels and joints to obtain desired motions and functions (e.g., deployable devices [23–25], printed circuit boards [26], and actuation origami [27–29]).

LEMs have been placed in series and parallel to facilitate desired behaviors of systems, and work has been done to characterize the global bending stiffness in the desired degree-of-freedom (DOF) [30]. When LEMs are placed in series and parallel, they have been termed lamina emergent arrays (LEAs) or compliant arrays [31]. LEAs also have compliance in other DOFs, and motion in these other DOFs has generally been termed parasitic and undesirable. Specific topological changes of joints, known as surrogate folds for origami-based mechanisms, have been designed to reduce the parasitic motion [32] to behave more like the kinematics of smooth folding structures [33].

This paper describes the formulation of arrays of LET joints (LET arrays, a subset of LEAs) suitable for origami-based mechanisms in which panel-area conservation is desirable and develops a load–displacement relationship set of analytical equations to describe the arrays in three DOFs in the elastic region. The behavior predicted by the theoretical approach is then verified via the finite element analysis (FEA). An integrated simulation environment [34], in which a MATLAB parametric script guides the computer-aided design (CAD) geometry generations as well as the structural batch simulations, is used to automatically test several LET arrays for each DOF. The rest of the paper is organized as follows: Sec. 2 gives a description of LET array formulations to be studied in this paper, Sec. 3 describes the theoretical load-deflection laws of the LET arrays for each of the considered DOF, Sec. 4 provides a comparison between theoretical and FEA results, and Sec. 5 summarizes the work and presents concluding remarks.

2 General Lamina Emergent Torsion Arrays

Figure 1 shows the joint frame and motions considered in this paper. We will refer to the rotation about the x-axis ($R_x(\gamma)$) as folding (referring to the origami-based engineering nomenclature), translation along the y-axis ($T_y(y)$) as extension/compression (or for brevity, extension), and rotation about the z-axis ($R_z(\beta)$) as in-plane rotation. LET joints were introduced as joints well-suited for high
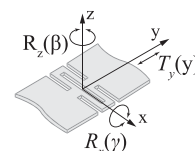
Fig. 1 Coordinate frame and motions considered

rotation in the desired folding motion and where some compliance in other DOF were also observed [13]. A single LET joint was defined as a specific formulation of four compliant torsion segments in series and parallel. Two possible configurations were presented as the Outside LET and the Inside LET which had the same four torsion segments with slight topological differences resulting in different boundary conditions of the segments. The differing boundary conditions affected the off-axis motion, but had no significant effects on the desired folding motion.

Researchers, to understand these motions, have developed models describing the load-displacement relationships for folding, extension, and in-plane rotation for single joints. A summary of their work is listed in Table 1. The table also shows the gaps in the literature that are important for origami-based design and this paper fills these gaps. Specifically, we give general equations which account for the various boundary conditions for the three DOF for general LET arrays with any combination of series, parallel, and configuration. Figure 2 illustrates motivations for filling these research gaps. Shown in the figure is a system of panels and joints that uses LET arrays to fold a large area into a small volume in the form of an origami pattern [23]. On the left is a close-up of these panels and joints, in the middle is the unfolded system, and on the right are details of the folded configuration. In the side view of the folded configuration, a close-up of a LET array is shown with displacements in the y-axis and about the x and z axes. It is this type of behavior which this paper characterizes to better understand how such systems of panels and joint perform.

Standard LET joints assume four torsion segments: two in series and two in parallel. Other formulations are possible, which include odd numbers of torsion segments. To reduce confusion when discussing LET arrays made up of torsion segments, we will drop the term LET joints when describing the topology of the arrays. Instead, we will refer to LET array topologies using the following convention: $SsPpc$. S is the number of torsion segments in series, P is the number of torsion segments in parallel, and c is the

Table 1 State-of-the-art of LET joint equations

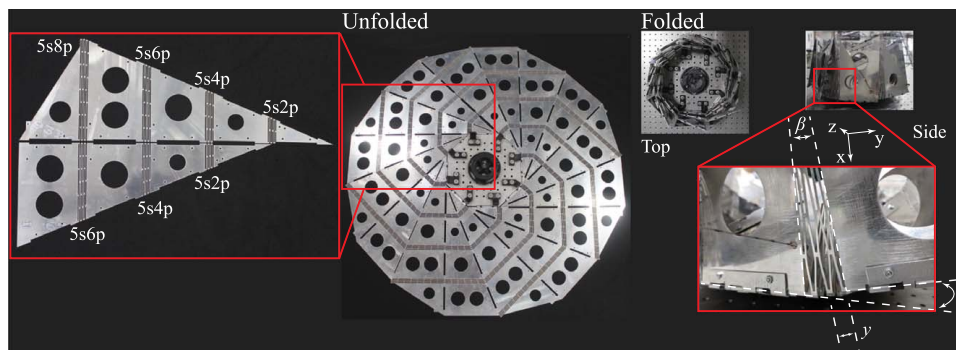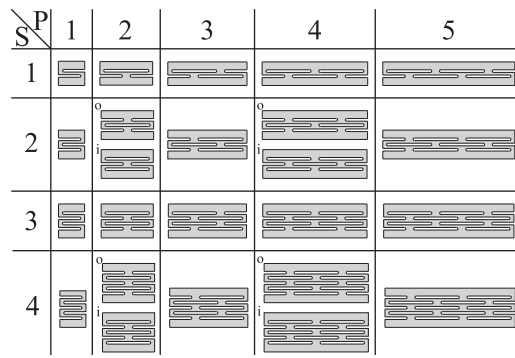|	Motion		
Joint	Folding (R_x)	Extension/ compression (T_y)	In-plane rotation (R_z)
Outside LET	Eqs. (1)–(4) [13], Eqs. (1)–(2) [35]	Eqs. (24)–(26) [13], Eqs. (1)–(3) [36]	Eqs. (3)–(11) [35], Eqs. (6)–(9) [36]
Inside LET	Eqs. (5)–(7) [13]	Eqs. (4)–(5) [36]	Eqs. (10)–(12) [36]
Full joint array	Eqs. (5)–(7) [31]	x	x
General array	x	x	x

Fig. 3 Possible serial–parallel topological formulations of LET arrays

configuration (whether the topology resembles an inside or outside LET joint, when applicable). For example, the designation 2s2pi is equivalent to an inside LET joint and 2s2po is the equivalent to an outside LET joint. A single torsion segment has the designation 1s1p and does not have a configuration c designation. Figure 3 shows possible formulations of LET arrays. The 2s2p location in the grid shows both configurations available to the 2s2p designation, with the outside LET on top and the inside LET on bottom. The outside/inside option is only available to designations with both even S and even P. The prototype shown in Fig. 2 indicates the LET array designations used in the left detail.

General LET arrays can be used to tailor stiffness values in different DOF while maintaining the ability to fold. For example, assuming the geometry of individual segments remain the same, LET arrays of the same S will have the same range of motion before failure in folding but will have different folding, extension, and in-plane rotation stiffness values, as is the case for the LET arrays indicated in Fig. 2. Note that, for example, LET arrays with a $P = 2$ formulation are equivalent to two separate LET arrays with a $P = 1$ formulation in terms of folding but are not necessarily equivalent in extension and in-plane rotation as the boundary conditions of the torsion segments can be different for each case. There are unlimited variations of formulating the compliant segments. This paper focuses on the topologies depicted in Fig. 3 for any S and P.

3 Load–Displacement Characterization

Load–displacement relationships (stiffness rates) for each of the three DOFs considered in this paper are given in this section. It is desirable in the design of systems of panels and joints to obtain equivalent stiffness rates, expressed as scalars, in each of the DOF for each joint. Throughout this section, fundamental dimensions are used and are labeled in Fig. 4. Torsion segments and bending segments are also indicated in the figure, about which will be discussed throughout the paper. l_T and w_T are the length
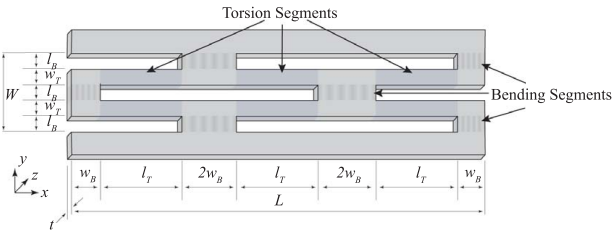

Fig. 2 Physical prototype of a system of panels and joints using LET arrays

Fig. 4 Representative dimensions of a 2s3p LET array

and width dimensions of torsion segments, respectively. l_B and w_B are the length and width dimensions of bending segments, respectively. L and W are the length and width dimensions of overall array, respectively, and are functions of the dimensions of the segments in bending and torsion. Throughout these analyses, we assume isotropic material properties. These relationships may also be applicable to symmetric and balanced laminate composites that exhibit isotropic behavior, but it is likely that other considerations, such as for coupling behavior, would be required.

While LET arrays with varying dimensions are possible, we assume that for a particular LET array, the bending and torsion segments, separately, are of equal dimensions and therefore stiffness. This assumption allows for simplification of the predictive models. However, if LET arrays of varying dimensions are to be designed, the following guidelines are suggested: (1) to avoid unnecessary stress risers, ensure that dimensions of the torsion segments are the same along any particular row and (2) treat rows of identical geometry as unique LET arrays and solve the displacement of each LET array in series.

3.1 Folding. We assume that the torsional stiffness k_T is the same for each torsion bar. We assume that the bending stiffness for each segment in bending on the outside of the array is k_B and that those on the inside of the array are twice as wide and therefore consists of two springs. A generalized analogous spring model is built by summing elements within rows in parallel and then the rows in series (Fig. 5). The resulting load–displacement relationship in folding for LET arrays is as follows:

$$M_x = K_{eq,rx}\gamma \tag{1}$$

where γ is the fold angle and $K_{eq,rx}$ is the stiffness rate found when adding the springs in parallel and in series:

$$K_{eq,rx} = \frac{Pk_T k_B}{S(k_T + k_B) + k_T} \tag{2}$$

A symmetric polar moment of inertia J_T equation for beam torsional stiffness k_T is given by [37]:
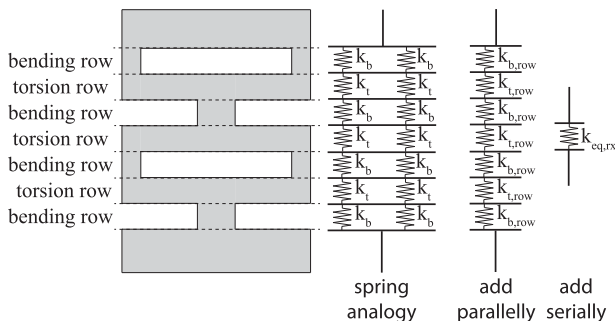
$$k_T = \frac{fJ_T G}{l_T} \tag{3}$$

where f is a compensation function [37] to ensure accuracy of a symmetric torsional stiffness J_T equation:

$$f = \frac{1.167z^5 + 29.49z^4 + 30.9z^3 + 100.9z^2 + 30.38z + 29.41}{z^5 + 25.91z^4 + 41.58z^3 + 90.43z^2 + 41.74z + 25.21} \tag{4}$$

and

$$J_T = \frac{2t^3 w_T^3}{7t^2 + 7w_T^2} \tag{5}$$

where $z = w_T/t$ and G is the modulus of rigidity of the material. The bending stiffness of the segments (Euler–Bernoulli) in bending is

$$k_B = \frac{EI_B}{l_B} \tag{6}$$

where E is the elastic modulus of the material and $I_B = w_B t^3/12$ is the moment of inertia of the segment in bending.

3.2 Extension/Compression. An outside LET torsion segment has a fixed-guided boundary condition, while inside LET torsion segment has a fixed-clamped condition. Here, we consider LET arrays that have a mixture of fixed-guided and fixed-clamped torsion segments, an example of which is shown in Fig. 6. The LET array has a 3s2p designation where four segments are fixed guided and two are fixed clamped. The differences between fixed guided and fixed clamped, in terms of loading conditions and mechanical responses, are discussed in Ref. [38].

To model the equivalent extension/compression spring stiffness $K_{y,eq}$ of LET arrays, we describe individual segment stiffness rates along the rows first (adding in parallel) and then across the rows (adding in series). Unlike the uniform distribution of stiffness rates for LET arrays in folding, LET arrays in extension/compression have a nonuniform distribution due to the mixed boundary conditions. Thus, additional row types are introduced as follows (see Fig. 7): a boundary row is a torsion row that contains a fixed-clamped segment, and if exists, it does so only at the transition from panel to joint (maximum of two in an array). A regular row is a torsion row that does not have fixed-clamped segments along the left and right edges of the array, and if exists, it may repeat (no maximum, but dependent on S). A bending segment row is composed of only bending segments. Figure 7 shows a LET array, which has two boundary rows, two regular rows, and five bending segment rows (as another example, the array in Fig. 6 has one boundary and two regular rows).
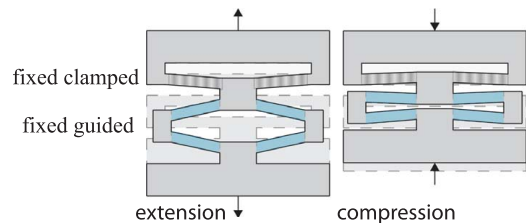

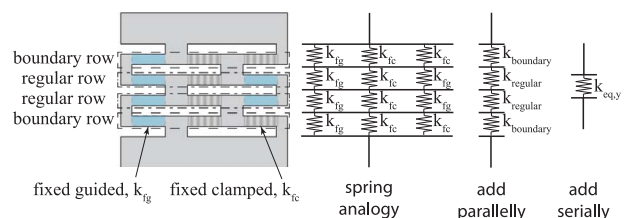**Fig. 6 Extension and compression of a 3s2p LET array**

Fig. 7 Spring analogy for extension and compression of a 4s3p LET array

Fig. 5 Spring analogy for folding of a 3s2p LET array

The force–displacement relationship is given as follows:

$$F_y = K_{y,eq}y \tag{7}$$

where y is in the direction indicated in Fig. 1, and the spring stiffness $K_{y,eq}$ for a LET array in extension/compression is as follows:

$$K_{y,eq} = \frac{k_{bound}k_{reg}k_{bend}}{n_{reg}k_{bound}k_{bend} + n_{bound}k_{reg}k_{bend} + n_{bend}k_{reg}k_{bound}} \tag{8}$$

where k_{bend} is the axial stiffness of bending segments:

$$k_{bend} = 2PE\frac{tw_B}{l_B} \tag{9}$$

and the number of bending segment rows is as follows:

$$n_{bend} = S + 1 \tag{10}$$

The number of boundary rows n_{bound} is as follows:

$$n_{bound} = \begin{cases} 0, & S \text{ is even and } P \text{ is even and } c = o \\ 1, & S = 1, \text{ or} \\ & S > 1 \text{ and } S \text{ is odd and } P \text{ is even} \\ 2, & S > 1 \text{ and } P \text{ is odd, or} \\ & S \text{ is even and } P \text{ is even and } c = i \end{cases} \tag{11}$$

For example, n_{bound} of the LET array in Fig. 7 is 2 because $S > 1$ and P is odd. The number of regular rows n_{reg} is as follows:

$$n_{reg} = S - n_{bound} \tag{12}$$

The boundary row force F_{bound} is

$$F_{bound} = k_{bound}y_{bound} \tag{13}$$

where y_{bound} is the displacement of the boundary row and the boundary row stiffness k_{bound} is

$$k_{bound} = n_{bfg}k_{fg}\big|_{y_{fg}=y_{bound}} + n_{bfc}k_{fc}\big|_{y_{fc}=y_{bound}} \tag{14}$$

where y_{fg} and y_{fc} are the displacements of fixed-guided and fixed-clamped segments, respectively, and the regular row force F_r is

$$F_r = k_{reg}y_r \tag{15}$$

where the regular row stiffness k_{reg} is

$$k_{reg} = n_{rfg}k_{fg}\big|_{y_{fg}=y_r} + n_{rfc}k_{fc}\big|_{y_{fg}=y_r} \tag{16}$$

where n_{bfg} is the number of fixed-guided segments in a boundary row:

$$n_{bfg} = \begin{cases} 0, & P \text{ is even, or} \\ & S = 1 \text{ and } P > 1 \text{ and } P \text{ is odd} \\ 1, & S > 1 \text{ and } P \text{ is odd, or} \\ & S = 1 \text{ and } P = 1 \end{cases} \tag{17}$$

For example, n_{bfg} of the LET array in Fig. 7 is 1 because $S > 1$ and P is odd. n_{bfc} is the number of fixed-clamped segments in a boundary row:

$$n_{bfc} = P - n_{bfg} \tag{18}$$

and where n_{rfg} is the number of fixed-guided segments in a regular row:

$$n_{rfg} = \begin{cases} 1, & P = 1 \\ 2, & \text{otherwise} \end{cases} \tag{19}$$

For example, n_{rfg} of the LET array in Fig. 7 is 2 because $P > 1$. n_{rfc} is the number of fixed-clamped segments in a regular row:

$$n_{rfc} = P - n_{rfg} \tag{20}$$

The stiffness coefficient k_{fg} of a fixed-guided beam assuming large deflections is nonlinear. Using equations for a fixed-guided beam from Ref. [9], a force–displacement relationship is found as follows:

$$F_{fg} = \frac{4K_T \arcsin\dfrac{y_{fg}}{\gamma_{fg}l_T}}{3\sqrt{\gamma_{fg}^2 l_T^2 - y_{fg}^2} - l_T(\gamma_{fg} - 1)} \tag{21}$$

where $K_T = 2\gamma_{fg}K_\Theta EI_y/l_T$ (the pseudo-rigid-body model (PRBM) spring constant for a fixed-guided beam) and γ_{fg} and K_Θ are the characteristic radius factor and the stiffness coefficient and are often approximated as 0.85 and 2.65, respectively [9]. E is the material modulus of elasticity and I_y is the area moment of inertia for the torsion segment in bending in the y-direction of the array ($tw_T^3/12$). The stiffness k_{fg} is the derivative of Eq. (21) with respect to y_{fg}:

$$k_{fg} = \frac{\partial F_{fg}}{\partial y_{fg}} \tag{22}$$

The stiffness coefficient k_{fc} of a fixed-clamped beam assuming large deflections is also nonlinear. The force–displacement relationship is as follows:

$$F_{fc} = \frac{K_A\Delta l_T\dfrac{\partial \Delta l_T}{\partial y_{fc}} + 2K_T\Theta_{fc}\dfrac{\partial \Theta_{fc}}{\partial y_{fc}}}{1 + \dfrac{L_T}{2}\dfrac{\partial \Theta_{fc}}{\partial y_{fc}}} \tag{23}$$

where K_A is the torsion segment axial stiffness:

$$K_A = \frac{EA_T}{\gamma_{fc}l_T + \Delta l_T} \tag{24}$$

where A_T is the axial cross-sectional area of the torsion segment as a function of elongation and Poisson's ratio ν:

$$A_T = tw_T\frac{l_T\left(1 + \dfrac{\Delta l_T}{l_T}(1 - 2\nu)\right)}{l_T + \Delta l_T} \tag{25}$$

where ΔL_T is the change in the length of the fixed-clamped beam:

$$\Delta L_T = \sqrt{\gamma_{fc}^2 l_T^2 + y_{fc}^2} - \gamma_{fc}l_T \tag{26}$$

and Θ_{fc} is the PRBM angle:

$$\Theta_{fc} = \arctan\frac{y_{fc}}{\gamma_{fc}l_T} \tag{27}$$

The kinematic coefficients are as follows:

$$\frac{\partial \Delta l_T}{\partial y_{fc}} = \frac{y_{fc}}{\sqrt{\gamma_{fc}^2 l_T^2 + y_{fc}^2}} \tag{28}$$

and

$$\frac{\partial \Theta_{fc}}{\partial y_{fc}} = \frac{\gamma_{fc}l_T}{\gamma_{fc}^2 l_T^2 + y_{fc}^2} \tag{29}$$

The stiffness k_{fc} value is the derivative of Eq. (23) with respect to y_{fc}:

$$k_{fc} = \frac{\partial F_{fc}}{\partial y_{fc}} \tag{30}$$

If there are both regular and boundary rows, respective displacements y_r and y_b are unknown because the stiffness values of the rows are nonlinear. Since the rows are assumed to be springs in series, the force is constant for each row:

$$F_b = F_r \tag{31}$$

and the regular row displacement can be parameterized as follows:

$$y_r = \frac{y - n_b y_b}{n_r} \tag{32}$$

such that the displacements y_r and y_b can be solved for using Eq. (31) as a function of joint displacement y. The evaluation of the force–displacement relationship is not straightforward. Algorithm 1 is presented for clarity.

Algorithm 1   Evaluating the force-displacement relationship F_y

---

1: Evaluate integers (Eqs. (9)–(12) and (17)–(20)
2: **for all** y **do**
3:    Formulate boundary row force F_b equation (substitute (Eqs. (22) and (30) (using Eqs. (23) and (24)–(26)) into Eq. (14)) into Eq. (13))
4:    Formulate regular row force F_r equation (substitute (Eqs. 22 and 30 (using Eqs. (23) and (24)–(26)) into Eq. (16)) into Eq. (15))
5:    Equate forces F_b and F_r (Eq. (31)), parameterize y_r (substitute Eq. (32) into Eq. (31)), and solve for y_b
6:    Evaluate row stiffness values k_b and k_r (Eqs. (14) and (16)) using updated y_b and y_r
7:    Evaluate equivalent spring stiffness $K_{y,eq}$ (Eq. (8)) by using updated row stiffness values k_b and k_r
8:    Evaluate force F_y (Eq. (7)) by using updated equivalent spring stiffness $K_{y,eq}$
9: **return** F_y

3.3 In-Plane Rotation. Different spring models are used for in-plane rotation of LET arrays for the cases when $P = 1$ and $P > 1$. For $P = 1$, moment-loaded beams are added in series. For $P > 1$, a proposed analogous spring model is developed. These cases are discussed below.

3.3.1 In-Plane Rotation When P = 1. For the case where $P = 1$, a moment–displacement relationship is found using a spring analogy of beams with moments applied at the end in series [9]:

$$M_z = K_{eq,rz}\beta \tag{33}$$

The equivalent spring stiffness rate is as follows:

$$K_{eq,rz} = \gamma K_\Theta \frac{EI_y}{l_T} \frac{1}{Sc_\theta} \tag{34}$$

where $\gamma = 0.7346$, $K_\Theta = 2.0643$, and $c_\theta = 1.5164$ for this case.

3.3.2 In-Plane Rotation When P > 1. A simplified spring model that assumes column extension/compression relative to a neutral axis is used to approximate the torque/displacement relationship of LET arrays of $P > 1$. Figure 8 illustrates how a particular LET array can be modeled as separate columns in extension and compression. Equivalent column spring stiffness values are found by adding rows of a column in series. A rotational displacement load is applied about the neutral axis, and the rotational displacement β causes extension/compression displacements in the columns resulting in column forces F_i. We assume small angles such that the columns remain vertical. These forces are multiplied by their respective distances from the neutral axis a_i and are
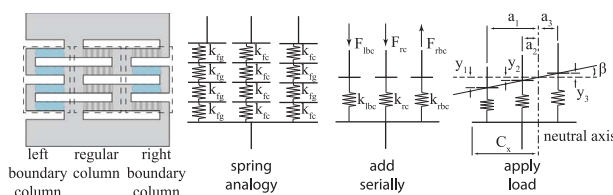

Fig. 8 Spring analogy for in-plane rotation of a 4s3p LET array

summed to equate to the resultant moment M_z:

$$M_z = \sum_{i=1}^{P} F_i a_i \tag{35}$$

The equivalent stiffness is as follows:

$$K_{eq,rz} = \frac{\partial M_z}{\partial \beta} \tag{36}$$

Each LET array formulation has a left boundary column and a right boundary column and has n_{rc} regular columns, where

$$n_{rc} = P - 2 \tag{37}$$

The column forces are composed of combinations of a left boundary column force F_{lbc}, regular column forces $F_{rc,i}$, and a right boundary column force F_{rbc}, resulting from displacements acting on the equivalent spring rates k_{lbc}, k_{rc}, and k_{rbc}, respectively. The left boundary column force F_{lbc} is equal to the force from a fixed-guided segment F_{lbcfg} or the force from a fixed-clamped segment F_{lbcfc}. They are as follows:

$$F_{lbcfg} = k_{fg}\big|_{y_{fg}=y_{lbcfg}} y_{lbcfg} \tag{38}$$

$$F_{lbcfc} = k_{fc}\big|_{y_{fc}=y_{lbcfc}} y_{lbcfc} \tag{39}$$

By parameterizing y_{lbcfg} as follows:

$$y_{lbcfg} = \frac{y_1 - n_{lbcfc}y_{lbcfc}}{n_{lbcfg}} \tag{40}$$

and by equating Eqs. (38) and (39), y_{lbcfc} can be solved for, similar to steps 5–6 of Algorithm 1. This process is repeated for the right column force, where

$$F_{rbcfg} = k_{fg}\big|_{y_{fg}=y_{rbcfg}} y_{rbcfg} \tag{41}$$

and

$$F_{rbcfc} = k_{fc}\big|_{y_{fc}=y_{rbcfc}} y_{rbcfc} \tag{42}$$

and where

$$y_{rbcfg} = \frac{y_1 - n_{rbcfc}y_{rbcfc}}{n_{rbcfg}} \tag{43}$$

Since the regular columns are composed of entirely of fixed-clamped segments, the resulting force can be evaluated directly as follows:

$$F_{rcfc} = \frac{1}{S} k_{fc}\bigg|_{y_{fc}=y/S} y \tag{44}$$

where y_{lbcfg} and y_{lbcfc} are the y displacement of fixed-guided and fixed-clamped segments, respectively, of the left boundary column; y_{rbcfg} and y_{rbcfc} are the y displacement of fixed-guided and fixed-clamped segments, respectively, of the right boundary column; and y_{rcfc} is the y displacement of fixed-clamped segments of the regular column. n_{lbcfc} is the number of fixed-clamped segments in the left boundary column:

$$n_{lbcfc} = \begin{cases} 0, & S \text{ is even and } P \text{ is even and } c = o, \text{ or} \\ & S \text{ is even and } P \text{ is odd} \\ 1, & S \text{ is odd} \\ 2, & S \text{ is even and } P \text{ is even and } c = i \end{cases} \tag{45}$$

n_{lbcfg} is the number of fixed-guided segments in the left boundary column:

$$n_{lbcfg} = S - n_{lbcfc} \tag{46}$$

where n_{rbcfc} is the number of fixed-clamped segments in the right boundary column:

$$n_{rbcfc} = \begin{cases} 0, & S \text{ is even and } P \text{ is even and } c = o \\ 1, & S \text{ is odd} \\ 2, & S \text{ is even and } P \text{ is even and } c = i, \text{ or} \\ & S \text{ is even and } P \text{ is odd} \end{cases} \quad (47)$$

and n_{rbcfg} is the number of fixed-guided segments in the right boundary column:

$$n_{rbcfg} = S - n_{rbcfc} \quad (48)$$

The moment arms a_i are the distances from the neutral axis C_x to the forces F_i. The neutral axis is found using

$$C_x = \frac{\sum_{i=1}^{P} F_i x_i}{\sum_{i=1}^{P} F_i} \quad (49)$$

where x_i is the distance from one side of the array to a column force:

$$x_i = \frac{l_T}{2} + w_B + (i-1)(l_T + 2w_B) \quad (50)$$

and a_i is given as follows:

$$a_i = |x_i - C_x| \quad (51)$$

and the y_i displacement for each column is given as follows:

$$y_i = a_i \sin \beta \quad (52)$$

The instantaneous spring rates (k_{fc} and k_{fg}) are the same as before (Eqs. (30) and (22)). Due to the nonlinearity of the spring rates, the neutral axis shifts as a function of displacement. Algorithm 2 is a proposed numerical algorithm to determine the location of the neutral axis, which is required to calculate the moment–rotation relationship. The values for γ_{fg} and γ_{fc} are substituted in γ_{fgz} and γ_{fcz}, respectively, for more accurate in-plane rotation results.

Algorithm 2   Locating the neutral axis C_x

1: **for all** β **do**
2:    $C_x \leftarrow \dfrac{L}{2}$ ▷ begin by assuming symmetry
3:    Solve for F_{lbc}, F_{rc}, and F_{rbc}
4:    **if** S is even and P is odd **then**
5:       Calculate $C_{x,new}$
6:       $\delta C_x \leftarrow |C_x - C_{x,new}|$
7:       $C_x \leftarrow (C_{x,new} + C_x)/2$
8:       **while** $\delta C_x > \epsilon$ **do**   ▷ ϵ is a predetermined convergence
                                    (i.e., $\epsilon = 1e^{-6}$ m)
9:          Solve for F_{lbc}, F_{rc}, and F_{rbc} using C_x
10:         Calculate $C_{x,new}$
11:         $\delta C_x \leftarrow |C_x - C_{x,new}|$
12:         $C_x \leftarrow (C_{x,new} + C_x)/2$
13:       **return** C_x
14:    **else**
15:       $C_x \leftarrow C_{x,new}$
16:       **return** C_x

---

4 Finite Element Analysis Comparison

To verify the analytical models, several LET arrays were tested using an integrated software framework [34], in which a MATLAB script manages the parametric study, a SOLIDWORKS macro updates the geometry of the LET arrays, and ANSYS APDL provides the force/torque–deflection characteristics of each configuration via batch mode. A routine, overseen by MATLAB, was defined to
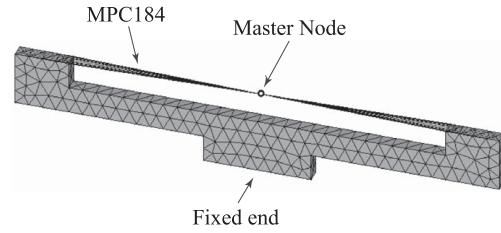

Fig. 9 Example of finite element model—1s2p LET array configuration

automatically export the CAD files from SOLIDWORKS and, subsequently, to perform the structural batch simulations of each candidate. In line with the proposed theoretical models, three DOFs were analyzed, namely $R_x(\gamma)$, $T_y(y)$, and $R_z(\beta)$. For each of the DOF, a free mesh with second-order tetrahedral elements ANSYS SOLID187 was defined with a maximum element size of t. This element type is particularly suitable for bending-dominated problems, where the shear locking effect is undesired due to its effect on the bending stiffness. In all simulations, the nonlinear geometry (NLGEOM) option was turned on. As for the employed material, aluminum alloy 7075 (heat treated) is considered, owing to its high strength-to-modulus ratio [9]. The Young's modulus and Poisson's ratio are, respectively, $E = 71.7$ GPa and $\nu = 0.33$. Concerning the boundary conditions, each LET array was fixed to the ground at one end and guided in a pure translation (along the y-axis) or rotation (about the x or z axes) on the other end. Since SOLID187 elements do not have rotational DOF, MPC184 elements were used to apply kinematic constraints (spider web of beams) between the solid model's nodes and a master node (as shown in Fig. 9), onto which rotational displacement loads can be applied. Referring to Figs. 2 and 4, the tested array parameters were $l_B = 2$ mm; $W_B = 4$ mm; $W_T = 2$ mm; $t = 1$ mm; $l_T = 10$ mm, $l_T = 20$ mm, or $l_T = 30$ mm; S (ranging from 1 to 3); P (ranging from 1 to 5); and c (either i or o, where applicable).

Figure 10 shows the force/torque–deflection relationships for arrays with $S = 2$, $l_T = 10$ mm and various P with the standard $\gamma = 0.85$. The modeled and FEA results have significant differences, with the modeled values higher than the FEA in each case, as shown in Fig. 11. For design, this may not be undesirable when considering strength. However, when considering behavior of systems that implement these types of arrays, more accurate predictions of the stiffness values are desired. A possible explanation for the overestimated stiffness is the inaccurately assumed boundary conditions. The fixed-guided and fixed-clamped boundary conditions do not account for the compliance of the bending segments or of the regions not modeled. Figure 12 shows an FEA strain plot of a 2s3p LET array, indicating the regions where forces and moments are transmitted, but whose spring models are not considered even though strain is observed. A more accurate representation of the overall deflection would include the compliance of these segments. One way to model this compliance in the T_y and M_z DOF is to modify the characteristic radius factor γ, effectively softening the assumed rigid boundaries of these regions (hence, the designated γ_{fg} or γ_{fc} variables in Eqs. (21), (23), and others). In the case of the arrays in Fig. 10, increasing the effective length of the torsion segment would decrease the array stiffness, bringing them closer to the FEA results. A way to model the compliance of these segments for the M_x DOF is to effectively lengthen the bending segments so that they "extend" into these regions, which we have done by adding $1/2w_T$ ($1/4w_T$ to both sides), making Eq. (14) equate to $k_B = E\, I_B/(l_B + 1/2w_T)$. By making these modifications, the errors between the FEA and modeled results are reduced (see Fig. 11). Table 2 lists the modified characteristic radius factors (e.g., γ_{fg}) used for the associated l_T and S values and their corresponding figures. In each row of the table, the only geometry variation was l_T. The radius factors listed in
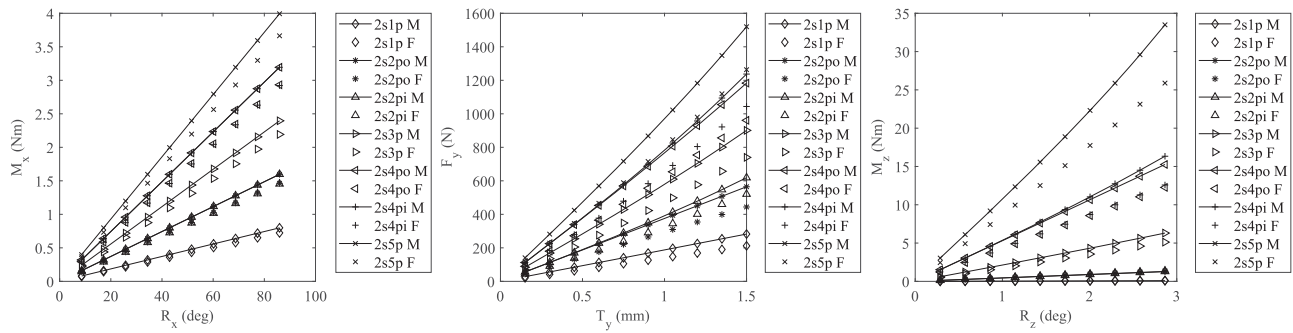
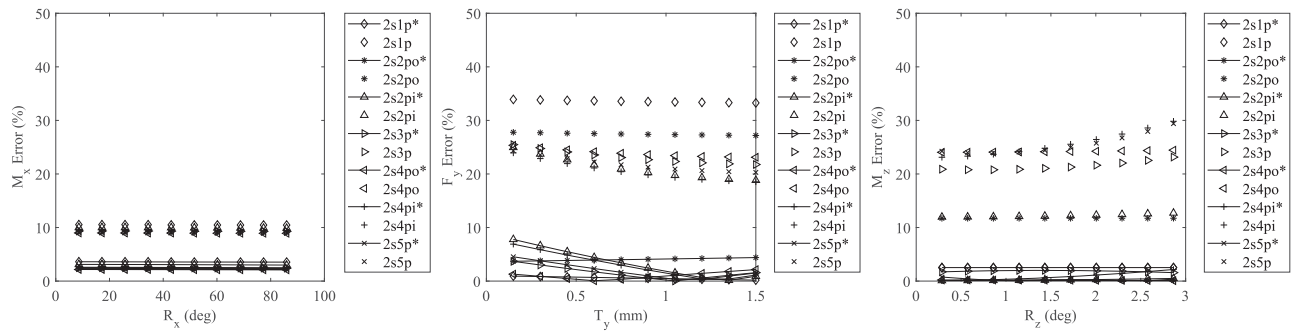**Fig. 10   Model and FEA load–displacement relationships for $S = 2$, $l_T = 10$ mm, various P, and the standard $\gamma = 0.85$**

Fig. 11   Errors before and after (indicated with *) modifications for $S = 2$, $l_T = 10$ mm, and various P
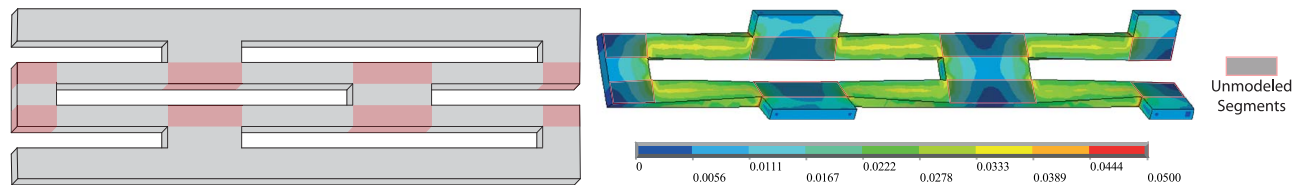

Fig. 12   Unmodeled segments and an FEA strain plot of a 2s3p LET array

Table 2   List of parameters, figures, and modified characteristic radius factors

l_T (cm)	γ_{fg}	γ_{fc}	γ_{fgz}	γ_{fcz}	S	Figure
1.0	1.29	1.06	1.18	1.16	1, 2, 3	13, 14, 15
2.0	0.74	0.73	0.64	0.82	1, 2, 3	16, 17, 18
3.0	0.61	0.64	0.48	0.80	1, 2, 3	19, 20, 21

the table were found using an optimization routine defined as follows:

$$\text{minimize} \quad \sum Error$$

$$\text{with respect to} \quad \gamma_{fg}, \gamma_{fc}, \gamma_{fgz}, \gamma_{fcz}$$

$$\text{subject to} \quad 0.1 \leq \gamma_{fg}, \gamma_{fc}, \gamma_{fgz}, \gamma_{fcz} \leq 2.0$$

$$\text{for each} \quad l_T \in \{1.0, 2.0, 3.0\} \text{ cm}$$

where *Error* is the absolute relative error of the load–displacement FEA and modeled results for each increment, DOF, and value of l_T:

$$Error = \left| \frac{T_{y,M} - T_{y,F}}{T_{y,F}} \right| \qquad (53)$$

where the subscripts M and F refer to modeled and FEA results, respectively, and R_z is substituted for T_y for the in-plane rotation DOF. The trend shows that for shorter torsion segments, the radius factors were increased from the standard 0.85 and that for longer torsion segments, the factors were decreased. By using the modified characteristic radius factors, the figures listed in Table 2 (i.e., Figs. 13–21, representing the load–displacement relationships for all the tested configurations) suggest that accurate stiffness estimates are achieved by using the presented model for LET arrays.

One exception to the modified radius factors listed in Table 2 was the case when $P = 2$ for the R_z DOF. The spring model presented in Sec. 3.3.2 assumes that the columns remain vertical during loading with the global rotation occurring as the left and right columns extend in opposite directions. For $P = 2$, however, there are no other segments in parallel to enforce vertical displacement, and so the model overestimates the stiffness by artificially enforcing the vertical constraint. Therefore, a separate optimization was performed for the case when $P = 2$ for each of the l_T values. The optimal radius factors were as follows: (for $l_T = 10$ mm) $\gamma_{fg} = \gamma_{fc} = 1.01$, (for $l_T = 20$ mm) $\gamma_{fg} = 0.53$ and $\gamma_{fc} = 0.56$, and (for $l_T = 30$ mm) $\gamma_{fg} = 0.40$ and $\gamma_{fc} = 0.49$. These values are especially useful when considering the traditional outside and inside LET joints (which are equivalent to 2s2po and 2s2pi LET arrays, respectively).
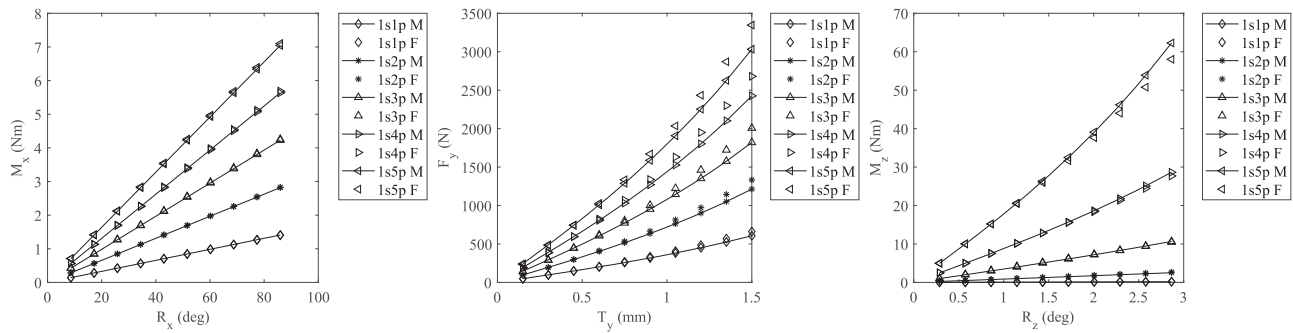
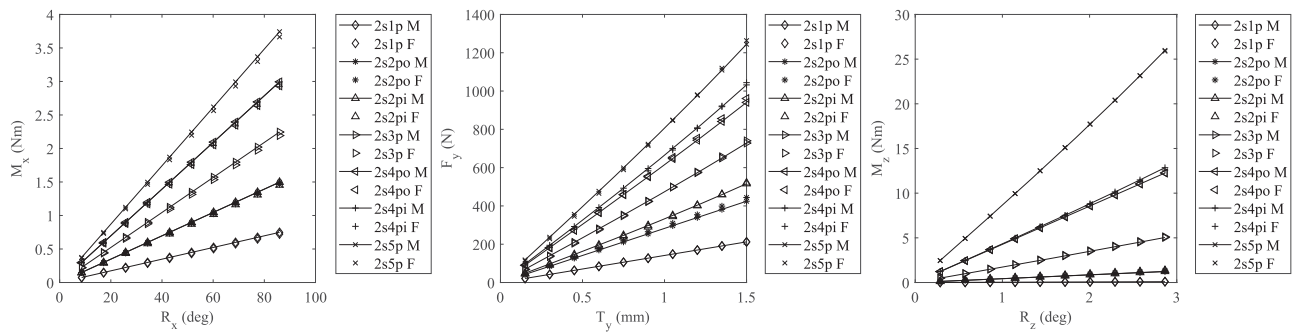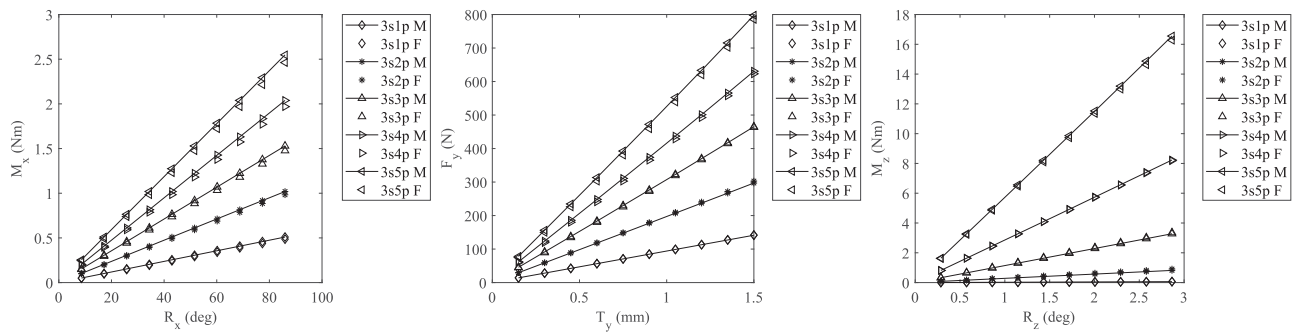**Fig. 13 Model and FEA load–displacement relationships for $S = 1$, $l_T = 10$ mm, various P, and modified γ values**

Fig. 14 Model and FEA load–displacement relationships for $S = 2$, $l_T = 10$ mm, various P, and modified γ values

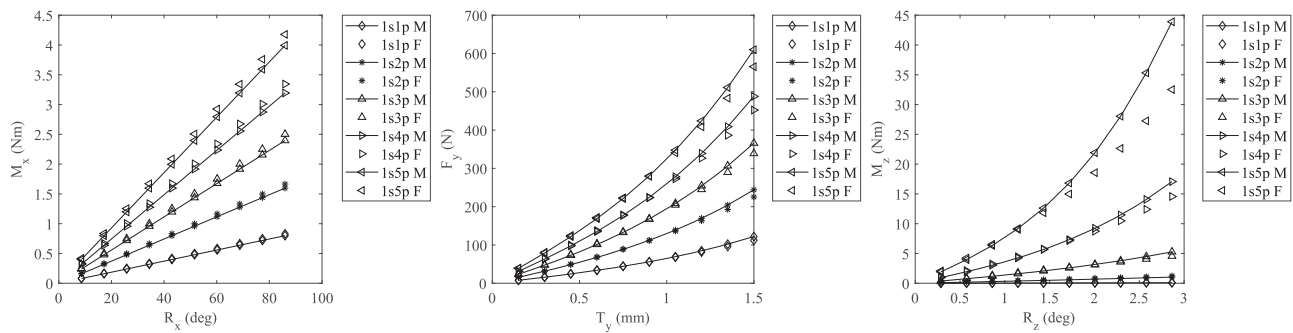**Fig. 15 Model and FEA load–displacement relationships for $S = 3$, $l_T = 10$ mm, various P, and modified γ values**

Fig. 16 Model and FEA load–displacement relationships for $S = 1$, $l_T = 20$ mm, various P, and modified γ values

It can be seen that for the T_y and R_z DOF, the force/torque–displacement relationships exhibit nonlinear behavior when S is low and P is high (see Figs. 13, 16, and 19) for both the FEA and modeled results. This is to be expected when considering the nonlinear terms in Eqs. (21) and (23) for these high-stiffness array formulations. It can also be seen that the errors are higher

for these cases, especially for the R_z DOF. A possible explanation for this error in the R_z model is that for these stiff cases, the simplifying spring models do not account for compliance at the boundaries and at the interactions between the bending and torsion segments. This inaccuracy in model assumptions is less apparent in the less-stiff and linear regimes of the arrays. Other
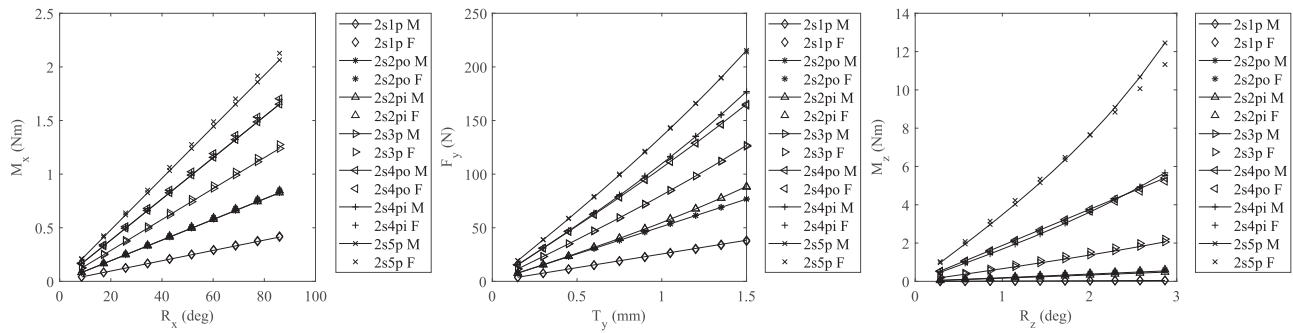
Fig. 17 Model and FEA load–displacement relationships for $S = 2$, $l_T = 20$ mm, various P and *config*, and modified γ values
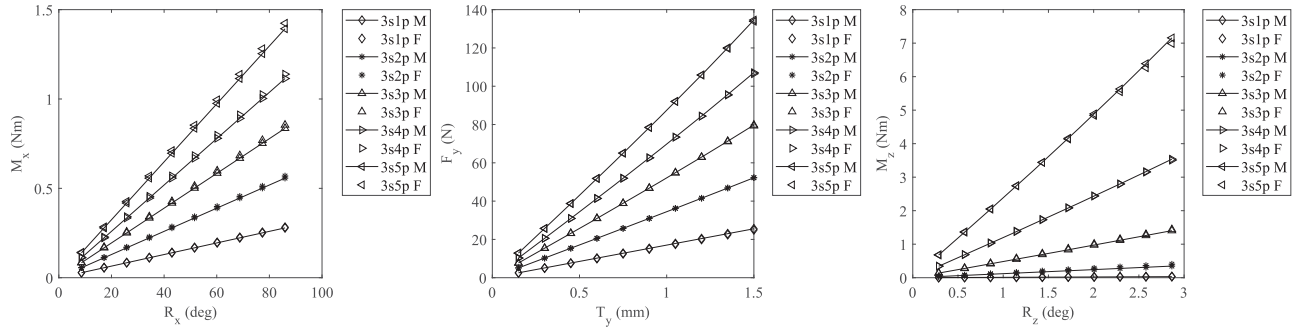

Fig. 18 Model and FEA load–displacement relationships for $S = 3$, $l_T = 20$ mm, various P, and modified γ values
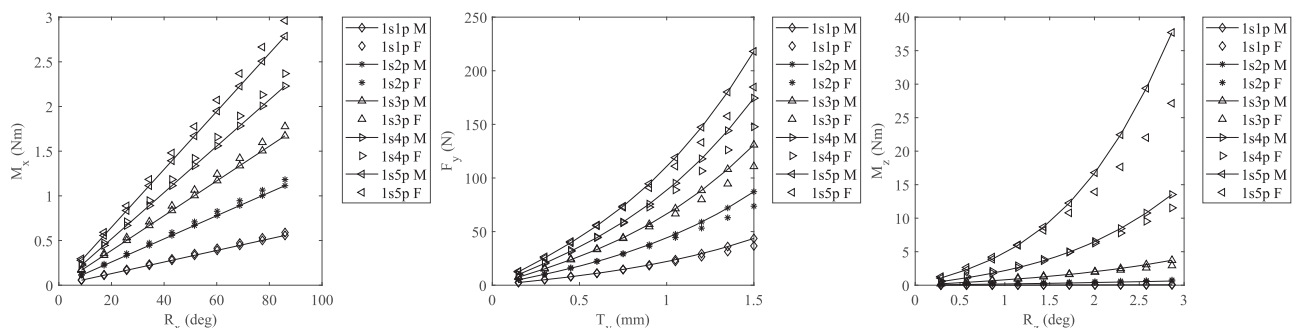

Fig. 19 Model and FEA load–displacement relationships for $S = 1$, $l_T = 30$ mm, various P, and modified γ values
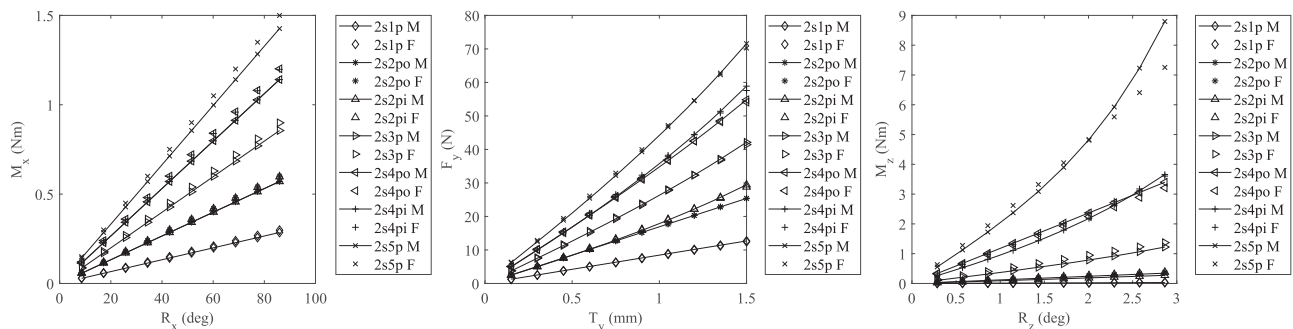

Fig. 20 Model and FEA load–displacement relationships for $S = 2$, $l_T = 30$ mm, various P and *config*, and modified γ values

cases (higher S) show excellent agreement between the analytical and FEA results.

The comparison between the FEA and modeled results verified that the models can accurately characterize general LET arrays for elastic load–displacement behaviors. These models represent an important tool for designers of systems that incorporate LET arrays to enable design of behaviors of such systems. The equations used assume the material to remain in the elastic region throughout the motion and are particularly useful in exploring the design space of the formulation of the
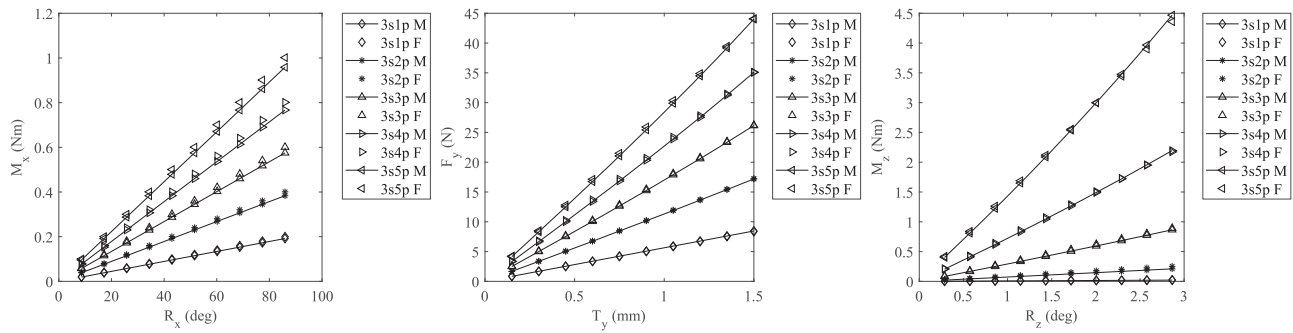
Fig. 21 Model and FEA load–displacement relationships for $S = 3$, $l_T = 30$ mm, various P, and modified γ values

LET arrays. When finalizing a design, consideration of the elastic limits is required. Equations of maximum stress of LET joints [13,39] can be applied to determine the stresses of LET arrays.

5 Conclusion

In this paper, LET arrays were defined as torsion segments in series and in parallel, which can be used for origami-based applications and others. The load–displacement relationships for the arrays were characterized in three DOFs enabling the design of arrays that consider off-axis motion.[1] The proposed models were verified using FEA for several LET array configurations resulting from an automatic framework. By using the standard $\gamma = 0.85$ value, conservative stiffness estimates are available. If more accurate stiffness estimated are desired, modified radius factors may be used. By using these modified values, load–displacement models had good agreement with the FEA results. Based on intuition and optimization results, shorter torsion segments may use higher γ values and longer torsion segments may use lower γ values. In some cases, the nonlinear behavior of the arrays were sources of error between the modeled and FEA results. Because the use of LET arrays is becoming more prevalent, the analytical models presented in this work enable their design. By using LET arrays, a designer can tailor the stiffness behavior for folding, extension, and in-plane rotation to realize folding and origami-based mechanisms. The provided stiffness values can be used for multibody dynamic or other system-modeling techniques in the design of such systems. By providing several plots of the force/torque–displacement relationships to show model verification, we have also showed the variability of the design space available to LET arrays.

References

[1] Jacobsen, J., Winder, B., Howell, L., and Magleby, S., 2010, "Lamina Emergent Mechanisms and Their Basic Elements," ASME J. Mech. Rob., **2**(1), pp. 1–9.

[2] Qiu, C., Qi, P., Liu, H., Althoefer, K., and Dai, J. S., 2016, "Six-Dimensional Compliance Analysis and Validation of Orthoplanar Springs," ASME J. Mech. Des., **138**(4), p. 042301.

[3] Qiu, L., Huang, G., and Yin, S., 2017, "Design and Performance Analysis of Double C-Type Flexure Hinges," ASME J. Mech. Rob., **9**(4), p. 044503.

[4] Qiu, L., Yin, S., and Xie, Z., 2016, "Failure Analysis and Performance Comparison of Triple-LET and LET Flexure Hinges," Eng. Failure Anal., **66**, pp. 35–43.

[5] Wang, R., and Zhang, X., 2017, "Optimal Design of a Planar Parallel 3-DOF Nanopositioner With Multi-Objective," Mech. Mach. Theory, **112**, pp. 61–83.

[6] Gollnick, P. S., Magleby, S. P., and Howell, L. L., 2011, "An Introduction to Multilayer Lamina Emergent Mechanisms," ASME J. Mech. Des., **133**(8), p. 081006.

[7] Alfattani, R., and Lusk, C., 2018, "A Lamina-Emergent Frustum Using a Bistable Collapsible Compliant Mechanism," ASME J. Mech. Des., **140**(12), p. 125001.

[8] Lobontiu, N., Gress, T., Munteanu, M. G., and Ilic, B., 2019, "Stiffness Design of Circular-Axis Hinge, Self-Similar Mechanism With Large Out-of-Plane Motion," ASME J. Mech. Des., **141**(9), p. 092302.

[9] Howell, L. L., 2001, *Compliant Mechanisms*, John Wiley & Sons, New York.

[10] Aten, Q. T., Jensen, B. D., and Howell, L. L., 2012, "Geometrically Non-Linear Analysis of Thin-Film Compliant Mems Via Shell and Solid Elements," Finite Elements Anal. Des., **49**(1), pp. 70–77.

[11] Francis, K. C., Blanch, J. E., Magleby, S. P., and Howell, L. L., 2013, "Origami-Like Creases in Sheet Materials for Compliant Mechanism Design," Mech. Sci., **4**(2), pp. 371–380.

[12] Pehrson, N. A., Magleby, S. P., Lang, R. J., and Howell, L. L., 2016, "Introduction of Monolithic Origami With Thick-Sheet Materials," Proceedings of the International Association for Shell and Spatial Structures Annual Symposium, Tokyo, Japan, Sept. 26–30, pp. 1–10.

[13] Jacobsen, J. O., Chen, G., Howell, L. L., and Magleby, S. P., 2009, "Lamina Emergent Torsional (LET) Joint," Mech. Mach. Theory, **44**(11), pp. 2098–2109.

[14] Xie, Z., Qiu, L., and Yang, D., 2017, "Design and Analysis of Outside-Deployed Lamina Emergent Joint (OD-LEJ)," Mech. Mach. Theory, **114**, pp. 111–124.

[15] Xie, Z., Qiu, L., and Yang, D., 2018, "Design and Analysis of a Variable Stiffness Inside-Deployed Lamina Emergent Joint," Mech. Mach. Theory, **120**, pp. 166–177.

[16] Saito, K., Tsukahara, A., and Okabe, Y., 2015, "New Deployable Structures Based on An Elastic Origami Model," ASME J. Mech. Des., **137**(2), p. 021402.

[17] Chen, Y., Sareh, P., Yan, J., Fallah, A. S., and Feng, J., 2019, "An Integrated Geometric-Graph-Theoretic Approach to Representing Origami Structures and Their Corresponding Truss Frameworks," ASME J. Mech. Des., **141**(9), p. 091402.

[18] Gillman, A. S., Fuchi, K., and Buskohl, P. R., 2019, "Discovering Sequenced Origami Folding Through Nonlinear Mechanics and Topology Optimization," ASME J. Mech. Des., **141**(4), p. 041401.

[19] Pradier, C., Cavoret, J., Dureisseix, D., Jean-Mistral, C., and Ville, F., 2016, "An Experimental Study and Model Determination of the Mechanical Stiffness of Paper Folds," ASME J. Mech. Des., **138**(4), p. 041401.

[20] Gao, W., Ramani, K., Cipra, R. J., and Siegmund, T., 2013, "Kinetogami: A Reconfigurable, Combinatorial, and Printable Sheet Folding," ASME J. Mech. Des., **135**(111009), p. 111009.

[21] Geiss, M. J., Boddeti, N., Weeger, O., Maute, K., and Dunn, M. L., 2019, "Combined Level-Set-XFEM-Density Topology Optimization of Four-Dimensional Printed Structures Undergoing Large Deformation," ASME J. Mech. Des., **141**(5), p. 051405.

[22] Bös, F., Wardetzky, M., Vouga, E., and Gottesman, O., 2016, "On the Incompressibility of Cylindrical Origami Patterns," ASME J. Mech. Des., **139**(2), p. 021404.

[23] Pehrson, N. A., Smith, S. P., Ames, D. C., Magleby, S. P., and Arya, M., 2019, "Self-Deployable, Self-Stiffening, and Retractable Origami-Based Arrays for Spacecraft," AIAA Scitech 2019 Forum, San Diego, CA, Jan. 7–11, Paper No. AIAA 2019–0484.

[24] Huang, H., Li, B., Zhang, T., Zhang, Z., Qi, X., and Hu, Y., 2019, "Design of Large Single-Mobility Surface-Deployable Mechanism Using Irregularly Shaped Triangular Prismoid Modules," ASME J. Mech. Des., **141**(1), p. 012301.

[1]To facilitate rapid implementation, a repository containing the proposed models for the LET array analysis can be downloaded from the source: http://dx.doi.org/10.17632/bvcjbcg3cs.1

[25] Zirbel, S. A., Lang, R. J., Thomson, M. W., Sigel, D. A., Walkemeyer, P. E., Trease, B. P., Magleby, S. P., and Howell, L. L., 2013, "Accommodating Thickness in Origami-Based Deployable Arrays," ASME J. Mech. Des., **135**(11), p. 111005.

[26] Defigueiredo, B. P., Zimmerman, T. K., Russell, B. D., and Howell, L. L., 2018, "Regional Stiffness Reduction Using Lamina Emergent Torsional Joints for Flexible Printed Circuit Board Design," ASME J. Electron. Packag., **140**(4), p. 041001.

[27] Fuchi, K., Buskohl, P. R., Bazzan, G., Durstock, M. F., Reich, G. W., Vaia, R. A., and Joo, J. J., 2015, "Origami Actuator Design and Networking Through Crease Topology Optimization," ASME J. Mech. Des., **137**(9), p. 091401.

[28] Guang, C., and Yang, Y., 2018, "An Approach to Designing Deployable Mechanisms Based on Rigid Modified Origami Flashers," ASME J. Mech. Des., **140**(8), p. 082301.

[29] Klett, Y., 2018, "PALEO: Plastically Annealed Lamina Emergent Origami," ASME IDETC/CIE International Design Engineering Technical Conferences and Computers and Information in Engineering Conference, Quebec City, Quebec, Canada, Aug. 26–29, p. V05BT07A062.

[30] Nelson, T. G., Bruton, J. T., Rieske, N. E., Walton, M. P., Fullwood, D. T., and Howell, L. L., 2016, "Material Selection Shape Factors for Compliant Arrays in Bending," Mater. Des., **110**, pp. 865–877.

[31] Nelson, T. G., Lang, R. J., Pehrson, N. A., Magleby, S. P., and Howell, L. L., 2016, "Facilitating Deployable Mechanisms and Structures Via Developable Lamina Emergent Arrays," ASME J. Mech. Rob., **8**(3), p. 031006.

[32] Delimont, I. L., Magleby, S. P., and Howell, L. L., 2015, "A Family of Dual-Segment Compliant Joints Suitable for Use as Surrogate Folds," ASME J. Mech. Des., **137**(9), p. 092302.

[33] Peraza Hernandez, E. A., Hartl, D. J., and Lagoudas, D. C., 2016, "Kinematics of Origami Structures With Smooth Folds," ASME J. Mech. Rob., **8**(6), p. 061019.

[34] Bilancia, P., Berselli, G., Bruzzone, L., and Fanghella, P., 2019, "A CAD/CAE Integration Framework for Analyzing and Designing Spatial Compliant Mechanisms Via Pseudo-Rigid-Body Methods," Rob. Comput. Integrated Manuf., **56**, pp. 287–302.

[35] Boehm, K. J., Gibson, C. R., Hollaway, J. R., and Espinosa-Loza, F., 2016, "A Flexure-Based Mechanism for Precision Adjustment of National Ignition Facility Target Shrouds in Three Rotational Degrees of Freedom," Fusion Sci. Technol., **70**(2), pp. 265–273.

[36] Chen, G., Magleby, S. P., and Howell, L. L., 2018, "Membrane-Enhanced Lamina Emergent Torsional Joints for Surrogate Folds," ASME J. Mech. Des., **140**(6), p. 062303.

[37] Chen, G., and Howell, L. L., 2009, "Two General Solutions of Torsional Compliance for Variable Rectangular Cross-Section Hinges in Compliant Mechanisms," Precision Eng., **33**(3), pp. 268–274.

[38] Howell, L. L., DiBiasio, C. M., Cullinan, M. A., Panas, R. M., and Culpepper, M. L., 2010, "A Pseudo-Rigid-Body Model for Large Deflections of Fixed-Clamped Carbon Nanotubes," ASME J. Mech. Rob., **2**(3), p. 034501.

[39] Chen, G., and Howell, L. L., 2018, "Symmetric Equations for Evaluating Maximum Torsion Stress of Rectangular Beams in Compliant Mechanisms," Chin. J. Mech. Eng., **31**(14), pp. 1–1.